Local and regional lunar regolith characteristics at Reiner Gamma Formation: Optical and spectroscopic properties from Clementine and Earth-based data

Patrick C. Pinet

UMR 5562 "Dynamique Terrestre et Planétaire," CNRS, Université Paul Sabatier, Groupe de Recherche de Géodésie Spatiale, Observatoire Midi-Pyrénées, Toulouse, France

Vladislav V. Shevchenko

Sternberg Astronomical Institute, Moscow

Serge D. Chevrel, Yves Daydou, and Christine Rosemberg

UMR 5562 "Dynamique Terrestre et Planétaire," CNRS, Université Paul Sabatier, Groupe de Recherche de Géodésie Spatiale, Observatoire Midi-Pyrénées, Toulouse, France

Abstract. A detailed remote sensing survey of the Reiner Gamma Formation (RGF) region by means of Earth-based telescopic and Clementine multispectral imaging has been made in the UV-visible-near-infrared domain. The spectral mixture analysis reveals the existence of three basic end-members relevant for modeling the observed spectral variations in the RGF vicinity. These are MB (mare background), SWS (southwest swirl), and RGS (Reiner Gamma soil). The first two components exhibit spectral characteristics consistent with a prevailing contribution of mature mare soils for the surroundings (MB) and of immature mare crater-like soils (RGS) at RGF. The third intermediate-albedo component (SWS) has general characteristics of a mature mare soil, but with a redder continuum slope. The reported observation can be modeled by a mechanism which would remove the finest fraction in the soil (particle diameter < 45 μm) at RGF and redistribute it in the vicinity with a laterally variable proportion and local accumulations such as at SWS site. According to the available set of in situ data documenting variations in the chemical composition, in the distribution of particle sizes, and in the degree of maturity with depth in the mare regolith, the characteristics depicted at RGF are those of a subsurface soil layer from a depth of the order of 0.3 - 0.8 m. In our view, the simplest way to account for the whole body of information available from the present work lies in the proposition that in the area of RGF the uppermost layer of the regolith has been optically and mechanically modified by a process involving the fall of fragments of a low-density cometary nucleus previously disrupted by tidal interaction in the Earth-Moon system. We recognize, however, that in the present state of knowledge, one cannot rule out the hypothesized existence of a zone of seismically modified terrain peripheral to the Imbrium or Orientale basins just beneath the mare surface that would be the actual source of the RGF magnetic anomaly.

1. Introduction

The distribution of lunar surface magnetic fields detected by planetary electron reflection magnetometry measurements of the Apollo 15 and 16 subsatellites suggested that the largest observed concentrations of lunar crustal magnetization occur antipodal to few relatively young large impact basins such as Imbrium, Orientale, Serenitatis, and Crisium [*Hood*, 1987; *Lin et al.*, 1988;

Hood and Williams, 1989]. The magnetometer and electron reflectometer experiment on the Lunar Prospector spacecraft has confirmed this conclusion. Electron reflection maps of the regions antipodal to the Imbrium and Serenitatis impact basins show that crustal magnetic fields fill most of the basin antipodal zones. This finding provides further evidence for the hypothesis that basin-forming impacts result in magnetization of the lunar crust at their antipodes [*Lin et al.*, 1998], as previously proposed on the basis of theoretical modeling [*Hood*, 1987]. In such a model, the generation of a magnetic concentration is caused by the expansion around the moon of the partially ionized vapor cloud produced in a hypervelocity basin-forming impact, forcing the preexisting ambient magnetic field to be concentrated for a brief time period in the antipodal zone. Magnetic remanence properties may then be

acquired during the period of compressed field amplification through several mechanisms, such as shock remanence by impact of solid secondaries ejected from the basin-forming event.

However, *Hood and Huang* [1991, p.9838] assume, on the basis of the work by *Lin et al.* [1988] and *Hood and Williams* [1989], that "the strongest individual magnetic anomalies in basin antipodal zones appear to be associated with swirl-like albedo markings similar in morphology to Reiner Gamma," the Reiner Gamma Formation (RGF) magnetic anomaly still stands as a particular case which may be caused by another type of event. Indeed, it is easy enough to be convinced that the observed magnetic anomaly associated with the albedo swirl is not a typical manifestation of a lunar crustal magnetic field. First, the extent of the magnetic anomaly occupies a relatively limited portion of the surface of the lunar sphere. While for Mare Marginis and Mare Ingenii the regions of swirl concentrations cover $\sim$ 74,000 and 50,000 km^2, respectively, the RGF region covers only $\sim$ 3300 km^2 [*Shevchenko*, 1994]. Such a size does not correlate with the scale of crustal structure of the Moon and with large-scale magnetic anomalies of the farside. Second, the antipodal area for RGF lies in an old cratered highland region within the farside centered around 7°S, 124°E. This region only contains old craters of intermediate sizes where there is no antipodal basin structure [*Lin et al.*, 1988]. Finally, the age of the relatively young large impact basins located at the antipodes of the regional lunar magnetic anomalies is $\sim$ 3.9 - 3.6 Gyr. However, the surface material related to the main feature of RGF is very immature, and the age of the RGF emplacement may be as recent as 10 Myr [*Shevchenko et al.*, 1993; *Shevchenko*, 1994].

RGF is an unusual high-albedo morphological lunar feature, with no topographic expression, approximately 30 x 60 km in extent, located in western Oceanus Procellarum, and its origin is still unresolved (Figure 1a). Three possible mechanisms for its formation have been invoked:

1. Its origin would be associated with unusually magnetic secondary crater ejecta from the nearby crater Cavalerius, or from the more distant Glushko (previously named Olbers A) crater [e.g., *Hood et al.*, 1979; *Hood and Schubert*, 1980]. In this line of thought, the magnetism of the formation would be generated by the cooling of shocked/heated ejecta fragments with abundant Fe^0 in the presence of a strong magnetic field. The RGF high albedo would result from the deflection of the solar wind by the magnetic anomaly which prevents the regolith from undergoing maturation processes [*Hood and Williams*, 1989].

2. Despite the RGF peculiarities mentioned above, its origin might be somehow related to that of other swirls observed on the farside in basin antipodal regions. Though a systematic antipodal correlation is not fully established, the recent Lunar Prospector magnetometer measurements at low altitude ($\sim$ 20 km) have revealed many localized magnetic anomalies with amplitudes comparable to the RGF one (tens of nanoteslas), some of them being correlated in location with swirls as characterized by their albedo markings [*Hood et al.*, 1999]. It is hypothesized [*Hood et al.*, 1981; L.L. Hood, personal communication, 1999] that there exists a zone of seismically modified terrain peripheral to the Imbrium or Orientale basins just beneath the mare surface that would be the actual source of the RGF magnetic anomaly. The RGF albedo marking would result from the emplacement of secondary crater ejecta excavated from shallow depths beneath the preexisting mare surface, this material being both exposed much more recently than the impact basins ejecta material and selectively shielded from the solar wind ion bombardment.

3. RGF could be related to the imprint of a recent cometary impact [G. P. *Kuiper*, lecture given to the Air Force Institute of Technology, Wright-Patterson Air Force Base, 1958; *Gold and Soter*, 1976; *Srnka and Schultz*, 1980; *Schultz and Srnka*, 1980; *Shevchenko*, 1984; *Hood and Vickery*, 1984; *Bell and Hawke*, 1987]. Accordingly, streamers of gas and dust in the inner coma struck the lunar surface at high velocity and produced an optical alteration and disruption of the upper layer of the regolith resulting in the occurrence of bright swirls with a spatial distribution due to the turbulence of the gas flow along the lunar surface and magnetic properties resulting from compression of the cometary field against the lunar surface.

Following earlier remote-sensing investigations of the spectral properties of the Reiner Gamma region by means of vidicon images and near-infrared spectra [*Bell and Hawke*, 1981; 1987], we reinvestigate the area by means of independent multispectral charge-coupled device (CCD) imaging observations aimed at characterizing the optical, photometric, and spectroscopic properties of the upper part of the regolith at subkilometric resolution.

2. Observation

A detailed remote-sensing survey of the region by means of Earth-based telescopic [*Pinet et al.*, 1992] and Clementine [*Nozette et al.*, 1994] CCD multispectral imaging has been made in the UV-visible-near-infrared domain (Figure 1), and the distribution of the main types of materials present in the vicinity of RGF is proposed on the basis of their photometric/spectral characteristics.

2.1. Photometric Observations

Using the brightness measurements obtained by the Zond-6 probe, integral albedo characteristics of the Reiner Gamma photometric structure and its immediate surroundings are derived. The reflectance values are found to range between 6 and 13% [*Shevchenko*, 1984].

Surface reflectance distributions are also estimated from the telescopic CCD (at 0.56 μm) and Clementine (at 0.75 μm) spectral data (see further in this section), these wavelengths reflecting also the regional surface albedo variations. If one builds up, for each photometric data set, the histograms corresponding approximately to the same region in the vicinity of RGF (see Figure 2), one obtains very similar polymodal distributions. These observed photometric distributions can be well described by the superposition of three normal Gaussian distributions, respectively centered on each mode (see Figure 2 and Table 1). The main one corresponds to the dark mare terrains. Of particular interest is the presence, within the RGF photometric structure, of local units displaying the same low integral albedo and reflectance values at 0.56 and 0.75 μm as the surrounding dark mare terrains. The second and third modes are related to intermediate-albedo surface units, surrounding RGF, and to the RGF central and brightest parts, respectively.

These independent observations clearly demonstrate that the photometric properties relative to usual mare regolithic soils are found regionally in this part of Oceanus Procellarum, but that local modifications occur in association with the formation of Reiner Gamma.

2.2. Spectral Observations

2.2.1. Comparison of different multispectral telescopic data sets. These telescopic datasets have been obtained on the 2 m aperture telescope of the Pic-du-Midi Observatory, France, in the course of two observational campaigns conducted during full-moon periods, in September 1990 and December 1992,
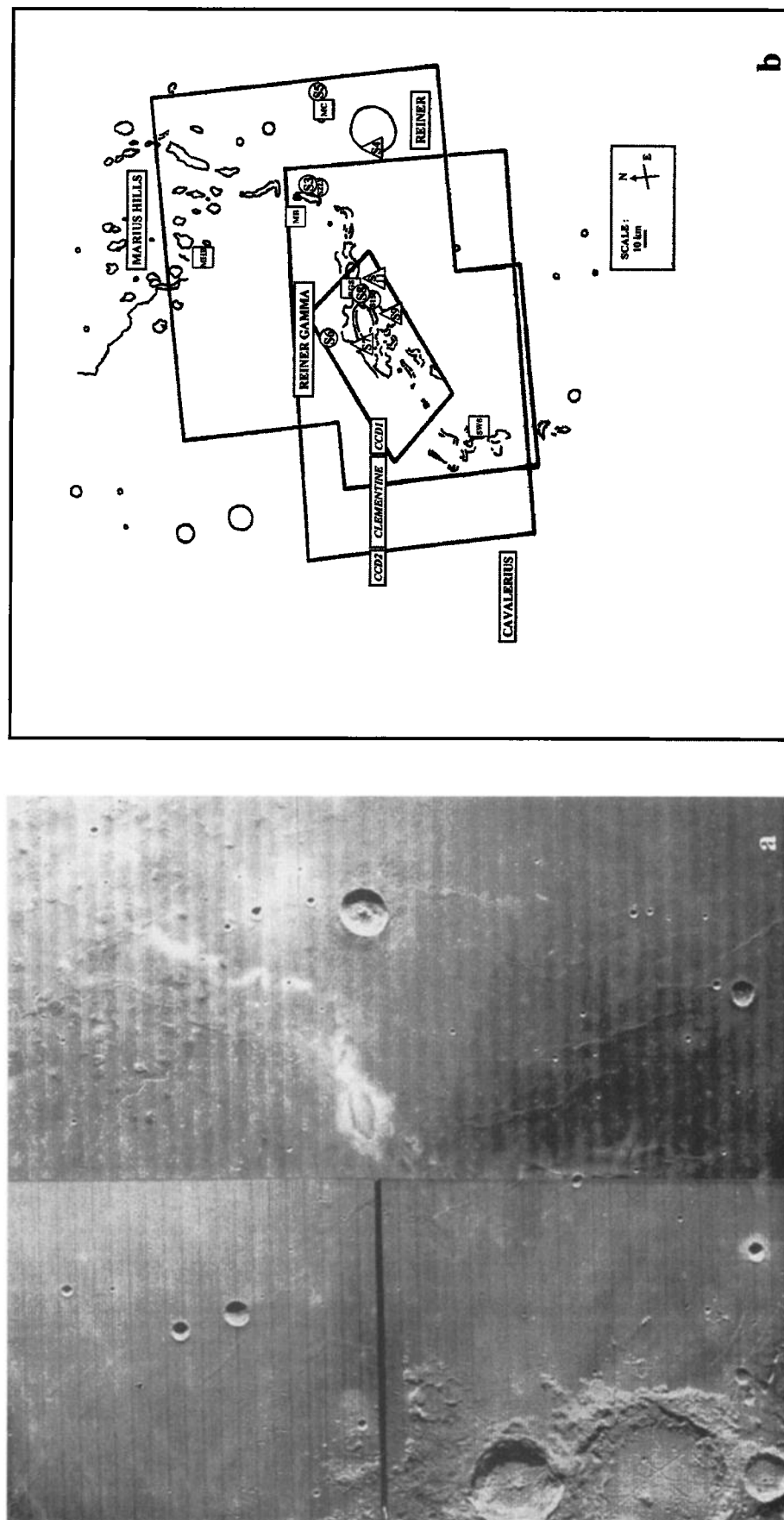
Figure 1. (a) Lunar Orbiter image of Reiner Gamma region. Frames: IV-157 and IV-162. (b) Regional setting of the different telescopic and Clementine multispectral mappings. Location of the reference spectra: Circles refer to the spectra from C.M. Pieters's atlas of spectra (1976) and from *Bell and Hawke* [1981, 1987] used for the radiometric calibration; triangles indicate spectra used for an independent control of its quality, estimated better than the 1% level on the scaled reflectance spectra. Squares indicate the location of the spectral end-members (see text and Plate 3). MHB, Marius Hills Basalt; MB, mare background; MC, mare crater; SWS, southwest swirl; CCD, charge-coupled device.
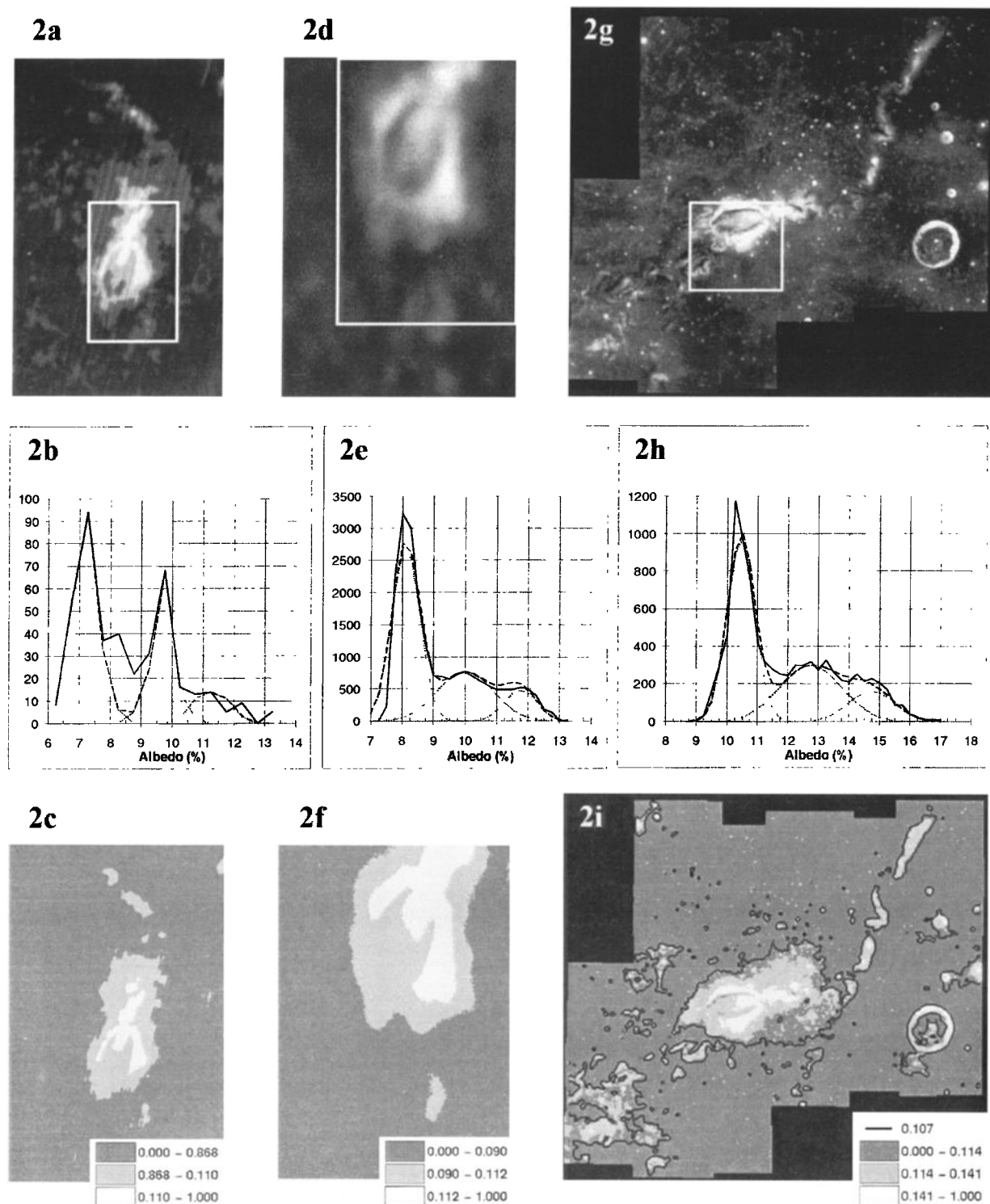
Figure 2. Photometric distributions associated with (a-c) Zond-6 image, (d-f) Earth-based telescopic image CCD1 taken at 0.56 µm, and (g-i) Clementine image taken at 0.75 µm. For Zond-6, the figures 2a, 2b, and 2c refer to the albedo image, the observed (solid lines) and modeled (dotted lines for each mode, dashed lines for the sum) distributions, and the spatial distribution associated with each mode (dark grey coding low-albedo range; pale grey, intermediate-albedo range; white, high-albedo range), respectively. Same for Figures 2d-2f and 2g-2i. The white rectangles drawn on Figures 2a, 2d, 2g indicate the zone where the photometric distribution is determined. For Figure 2i, the solid line corresponds to isophote 0.107 (see section 3 in relation to the "red halo" identification and southwest swirl SWS end-member contribution in Plate 3c).

Table 1. Parameters of the Three Normal Gaussian Distributions, Describing the Observed Polymodal Photometric Distributions

i	A_m	σ	Δ	λ	$p(\lambda)$
			Zond		
1	7.25	0.85	0.569	0.458	0.995
2	9.75	0.75	0.329	0.367	0.999
3	11.25	1.01	0.102	0.321	1.000
			CCD1		
1	8.10	0.54	0.569	0.127	1.000
2	10.00	1.03	0.318	0.141	1.000
3	11.75	0.61	0.112	0.112	1.000
			Clementine		
1	10.45	0.55	0.524	0.044	1.000
2	12.75	1.15	0.336	0.080	1.000
3	14.75	0.90	0.140	0.036	1.000

See Figure 2. Parameters are as follows: i, mode number; A_m, albedo of the mode; σ, standard deviation; Δ, distribution relative weight; λ, parameter of the Kolmogorov criterion; $p(\lambda)$, probability that the theoretical distribution explains satisfactorily the observed distribution according to Kolmogorov criterion.

respectively. The multispectral data have been instrumentally calibrated following the procedure described elsewhere [e.g., *Chevrel and Pinet*, 1992], and the images corresponding to a given set have been coregistered by bidimensional correlation [*Pinet et al.*, 1993], the overlapping independent frames being numerically mosaicked. Then a radiometric calibration has been made using telescopic and Galileo spectra (Figure 1b) [*Pieters*, 1986, 1993; *Bell and Hawke*, 1981, 1987; *Gaddis et al.*, 1995]. It resulted in the production of absolute reflectance spectra, and reflectance spectra relative to MS2 (Mare Serenitatis-2 standard) scaled to unity at 0.73 or 0.75, and 1.02 or 1.00 µm, depending on the telescopic or orbital considered data set, respectively. The consistency between the different data sets is within 2%. The two telescopic data sets (CCD1 (THX 384 x 576 array) and CCD2 (THX 1024 x 1024 array)) comprise 10 (0.4, 0.56, 0.73, 0.91, 0.95, 0.97, 0.98, 0.99, 1.02, and 1.05 µm) and 7 (0.56, 0.73, 0.91, 0.95, 0.98, 1.02, and 1.05 µm) narrow spectral bands, respectively, with a 100 Å bandwidth and a 1 km true spatial resolution [*Pinet et al.*, 1992]. The respective image fields are shown in Figure 1b, where the wide frame corresponds to the CCD2 frame and the small one corresponds to the CCD1 image.

A principal component analysis is carried out on each data set. Principal component analysis (PCA) is an analytical technique based upon a transformation of spectral axes such that variability is maximized. PCA is quite efficient with remote-sensing data for which some channels may be highly correlated [e.g., *Cloutis*, 1996] as it determines the useful dimensionality of the data set and allows one to understand how the data cloud distribution is clustered in the factor spaces [*Pinet et al.*, 1995a,b]. Looking at the topology of the statistical cloud in the principal component's (PC's) space, mean spectra are produced for the main spectral

components, which are shown with their spatial distribution. It emphasizes the identification of the extreme spectral types and of the possible mixing trends (each spectrum retrieved from the image cube is located as a single point in the principal component space). It reveals that : (1) RGF presents surface materials reflectance spectra (Plate 1) with spectral characteristics close to those of immature mare craters. However, these spectra coded in red, blue, and yellow show some variations in the UV (0.4-0.56 µm slope) and the 1 µm range; their spatial distribution correlates with the photometric anomaly previously mapped [*Shevchenko*, 1984]. (2) The RGF immediate surroundings show the presence of a specific intermediate-albedo spectral component (Plate 1), in agreement with the proposition made previously of the existence of a "red halo" unit [*Bell and Hawke*, 1987]. It is also distributed in a more diffuse way in the surrounding mare region, with a concentration of local patches mainly southward of the formation. It has general characteristics of a mature mare soil, but with a slightly redder continuum slope and a slope change in the visible (Plate 1b; spectrum in blue). However, the slope in scaled reflectance relative to MS2 appears almost flat (Plates 1c and 1h). Depending on the scaling wavelength (either 0.73 (Plate 1c) or 0.56 µm (Plate 1d)), the relative behavior in the UV-visible domain between the immediate mare surroundings and RGF spectra is modified within 3-5%, suggesting that a relative effect in soil maturity is involved [*Johnson et al.*, 1991b; *Fisher and Pieters*, 1994, 1996]. (3) The general background is composed of mare mature soils (Plates 1b and 1g; spectrum in magenta). (4) The PCA plot (Plate 1f) corresponding to CCD2 image (Plate 1i; location given by the CCD2 frame in Figure 1b) demonstrates that there is no component from Cavalerius crater ejecta (lower left corner in Plate 1i and lower right wing in Plate 1f) present in
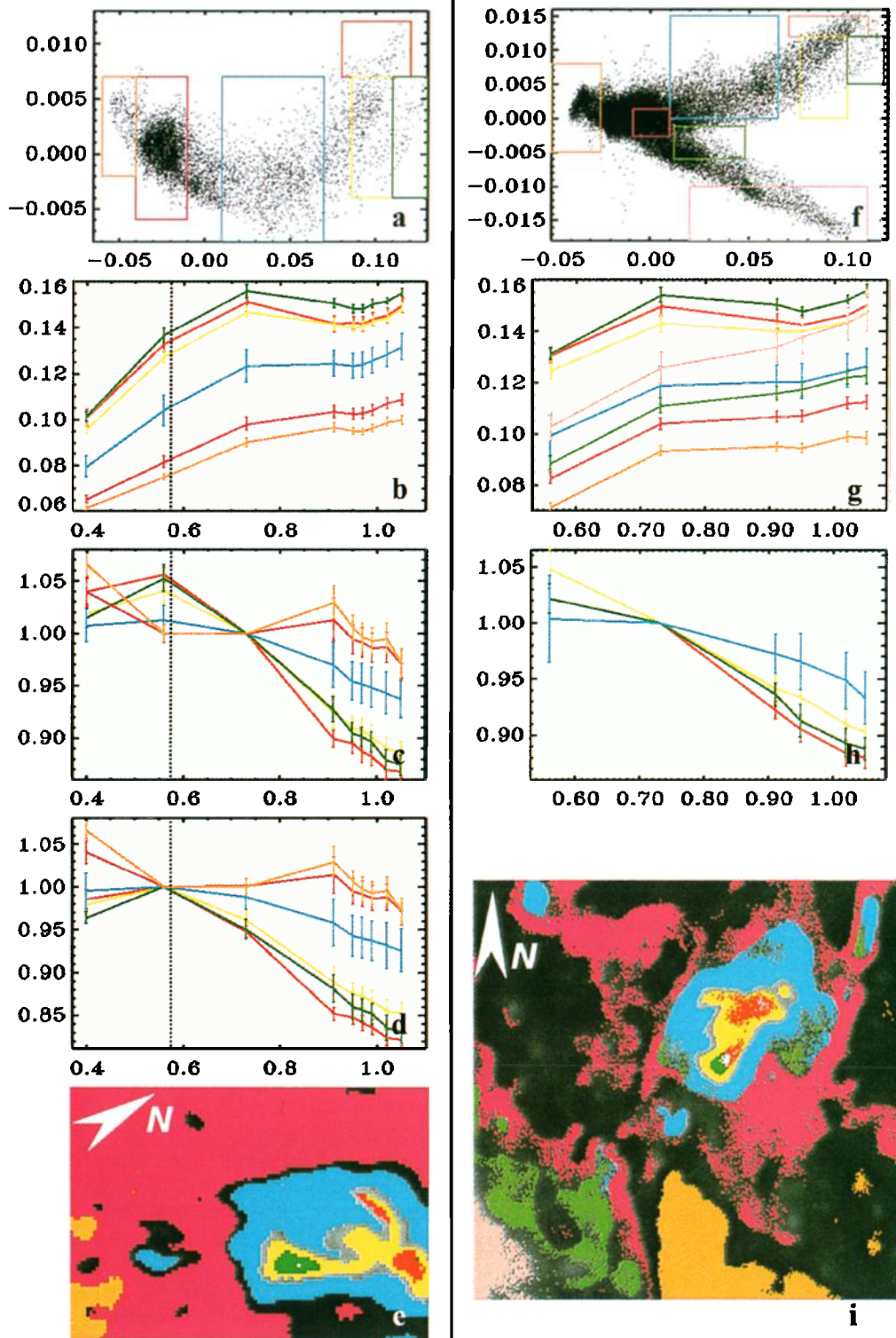
Plate 1. Earth-based telescopic multispectral observations of Reiner Gamma Formation from Pic-du-Midi Observatory. (a) PCA analysis of CCD1 multispectral image represented in the projection space of the first and second principal axes, (b) reflectance spectra related to the PCA boxes for CCD1, (c) corresponding spectra relative to MS2 standard and scaled at 0.73 μm for CCD1, (d) same as (c) but scaled at 0.56 μm, (e) spatial distribution associated with the different PCA boxes for CCD1, (f) PCA analysis of CCD2 multispectral image represented in the projection space of the first and second principal axes, (g) reflectance spectra related to the PCA boxes for CCD2, (h) corresponding spectra relative to MS2 standard and scaled at 0.73 μm for CCD2, and (i) spatial distribution associated with the different PCA boxes for CCD2.

Reiner Gamma Formation (Plate 1f: upper right wing, and Plate 1i); this observation discards the possibility of a spectral mixture involving Cavalerius material to explain the observed spectral characteristics of Reiner Gamma swirls.

CCD-spectropolarimetric images produced in total light and at wavelengths 0.56 and 0.73 μm also revealed the specific behavior of the RGF unit [Pinet et al., 1995a]. Again, the red halo unit has polarimetric properties which differ from both the mare surroundings and RGF. Local patches spatially associated with bright areas considered above to be part of the Reiner Gamma swirls have polarimetric properties identical to the red halo unit, some of these patches having in their central part polarimetric properties close to the RGF anomaly. Observed variations were interpreted as related to soil maturity and/or grain size distribution [Pinet et al., 1995a].

2.2.2. Clementine UV-VIS multispectral data analysis.

Following the Reiner Gamma region telescopic exploration described in section 2.2.1, a detailed remote-sensing survey of the region of Oceanus Procellarum surrounding RGF has been carried out by means of Clementine UV-VIS imaging data. The purpose is to establish the regional distribution of the maturity index and weight percent of iron content in the lunar soils.

2.2.2.1. Processing: The Clementine data (CCD THX 384 x 288) comprise five bands (0.41, 0.75, 0.90, 0.95, and 1.00 μm), with a 50-200 Å bandwidth and a 200 m spatial resolution [Nozette et al., 1994]. Each spectral image has been instrumentally calibrated (i.e., dark-field and flat-field corrected), registered, and mosaicked through the ISIS procedures established by the Clementine team (see Clementine basemap mosaic of A.S. McEwen et al. (unpublished data, 1997)). The resulting mosaic comprises 25 independent frames, each acquired in five bands. The coverage has been defined on the basis of our previous regional telescopic observation, in order to best focus on the regional variability related to RGF. The internal consistency after processing of the overall mosaic is better than 2% in absolute reflectance within each band, though some residual defects may still be seen in a few overlapping areas. Given the fact that the lunar photometric function is not yet fully established for all wavelengths [McEwen, 1996], we have chosen to derive a regional photometric calibration on the harmonized Clementine mosaic through an empirical line method [Smith et al., 1990a, b], relying on a number of previous telescopic and Galileo spectra (spectra 3, 4, and 5 in Bell and Hawke [1981, 1987], C.M. Pieters (unpublished atlas, 1976), Pieters [1993], Gaddis et al. [1995]). The result is the production of absolute reflectance spectra (and reflectance spectra relative to the MS2 standard and scaled to unity at 0.75 micron), organized in an image cube corresponding to the mosaic displayed in Figure 2g and Plate 2. These reflectance spectra are normalized to the reflectance of Apollo 16 soil 62231 under laboratory conditions, and their photometric accuracy estimate is ~ 2-3%.

2.2.2.2. Effect of soil maturity versus iron composition on the optical local variations: Since the previous studies suggest that the surface reflectance variations observed at Reiner Gamma region might be ascribed to a combination of both optical and compositional effects occurring in the regional mare regolith, our first objective is to assess their relative contributions. Indeed, iron dominates the broadband reflectance properties of the lunar surface, with iron occurring in the form of metallic iron and Fe^{2+} ion in minerals and glasses. Reflectance properties of lunar spectra are sensitive, for one part, to the mineralogical and elemental abundances, and for the other part, to the physical processes,

called soil maturation, occurring in the lunar regolith with exposure to solar wind and micrometeorite bombardment. Maturation process includes impact comminution, accumulation of agglutinates, and production of reduced iron from vacuum reduction of Fe^{2+} in minerals and glasses in the presence of hydrogen and carbon implanted by the solar wind. As a result, the lunar surface materials darken, redden, and lose spectral contrast with increasing maturity. Increasing the mineralogical Fe^{2+} abundance in the surface materials decreases the reflectance of minerals and increases the spectral contrast. Disentangling these respective contributions due to soil maturity and iron content has long been a central issue in lunar spectroscopic studies [e.g., Fisher and Pieters, 1994, 1996]. Only recently, a quantitative reliable method has been proposed [Lucey et al., 1995, 1998; Blewett et al., 1997] which can be applied to Clementine spectral data. This method shows that on the basis of the examination of a suite of Apollo lunar soil samples, one can empirically separate both effects (soil maturity and iron content) in the lunar soil spectral properties in a rather simple way. As a matter of fact, if one considers the spectral ratio 0.95/0.75 μm as a function of the reflectance at 0.75 μm, one shows that both effects are orthogonal and can be described by polar coordinates (ρ, θ), the iron content variation corresponding to the angular parameter and the maturity trend corresponding to the radial parameter; the larger the θ, the higher the iron content in the soil, and the higher the ρ, the more immature the soil.

Such an approach is utilized on the Clementine Reiner Gamma mosaic. A systematic analysis of the spatial distribution of the spectral features in the image is then performed, based on the examination of soil maturity variations, for a given iron content (wt %), considered as a class. The results are summarized and displayed in Plate 2. The regional variations can be described according to three classes, which are shown in Plates 2a-2d, 2e-2h, 2i-2l. For each class are given the location of the considered boxes in the $(\rho$, soil maturity parameter; θ, iron content parameter) space, the associated spatial distributions, and the corresponding average spectra both in reflectance and relative to MS2, scaled at 0.75 μm. Converting into Fe content [Lucey et al., 1995] indicates that the three classes correspond to a rather limited iron content variation, in the range of 2 wt%. However, they reveal an interesting spatial distribution. Class 1 refers to the regional mare basalt regolith in general (Plates 2a-2d); class 2 refers to the immediate mare background surrounding Reiner Gamma Formation (Plates 2e-2h) and class 3 appears to be predominantly related to RGF and the elongated bright structure, northeast of Reiner Gamma (Plates 2i-2l). Ejecta at the periphery of regional impact craters such as Reiner also belong to this class but show a lesser degree of relative immaturity than the Reiner Formation. In relation to the three classes so defined, one notes a progressive trend from relatively mature (class 1) toward relatively immature soils (class 3). Indeed, the ρ parameter ranges from 0.15 to 0.28 for class 1, from 0.18 to 0.30 for class 2, and from 0.20 to 0.40 for class 3. The uppermost tail, at the extreme right in the (ρ, θ) plot, is not represented here and corresponds to the very immature regolithic soils associated with the brightest small mare impact craters.

From the examination of the characteristics of the associated spectra and their location in the (ρ, θ) plot, we select five extreme spectral types displayed in Plates 2m and 2q with stars. The examination of the topology of the statistical cloud, corresponding to the projection of the Clementine UV-VIS data along the first two principal axes bearing 99.4% of the total variance reveals that

these types are extreme and are associated with different trends or "fingers" in the projection of the PCA cloud shown in Plate 2q. These types are used in a supervised classification process, based on the notion of topological neighborhood in the PC's space derived from the maximum likelihood classification technique, for mapping the related units present in the scene [*Chevrel et al.*, 1999].

The red-coded (Marius Hills basalt (MHB), Plates 2m-2q) unit is clearly related to morphological units belonging to the Marius Hills volcanic complex. Spectra indicate very low albedo terrains, high UV/VIS ratios (relative to MS2) in the range of 1.09-1.10 (Plate 2o), concave-down inflection in the near-infrared, and thus very weak absorptions at 1.0 μm. These spectral characteristics are consistent with very mature high-titanium mare basalt soils. The green unit (mare basalt background soil (MB) in Plates 2m-2q) appears to be representative of the regional mare background. Its average spectrum indicates an intermediate UV/VIS ratio in the range of 1.03-1.04, corresponding to 3 wt % TiO_2 content, in agreement with general estimates for this part of Oceanus Procellarum from telescopic observations [e.g., *Johnson et al.*, 1991a, b]. It also shows a weak 1 μm band absorption. Though slightly brighter in albedo, the yellow unit has also mare-like spectral characteristics and has indeed a very flat spectrum relative to MS2 (Plate 2o). It correlates spatially with swirl-like structures seen in the south-west of Reiner Gamma Formation and corresponds to a specific trend in the PCA diagram (SWS in Plates 2m-2q).

The blue unit (Reiner Gamma Formation soil (RGS) in Plates 2m-2q) depicts the brightest features in RGF, presumably related to small impact craters on the Reiner Gamma pattern. It has very similar UV/VIS ratio to that of the mare background (green unit) but presents a deep absorption at 1 μm (1.00/0.75 μm ratio of the order of 0.82) relative to MS2, consistent with the presence of immature mare soils [*McEwen et al.*, 1993]. Finally, the fresh mare craters and very immature parts of the Reiner crater rim are represented by the pink spectrum (fresh mare impact crater (MC) in Plates 2m-2q).

2.3. Spectral Mixture Modeling

Spectral mixture analysis has gained wide acceptance in the past years and is used to separate the spectral components of lunar soils, mixed at the pixel scale, into percentages of distinct end-members [e.g., *Bell and Hawke*, 1987; *Adams et al.*, 1986; *Pinet et al.*, 1993; *Head et al.*, 1993]. However, the use of simple linear mixing models is hampered by the arbitrary selection of end-members relevant to the geological problem under investigation. Different alternative approaches have been proposed [e.g., *Boardman*, 1993; *Tompkins et al.*, 1994; *Merényi et al.*, 1996; *Tompkins*, 1997]. Following previous works [*Johnson et al.*, 1994; *Pinet et al.*, 1995b, 1996; *Martin et al.*, 1997], we have developed a methodology which combines principal component analysis (PCA) and iterative linear mixture modeling (ILMM). It permits one to (1) to select the most representative end-members of a particular region, in terms of spatial distribution and spectral units (Indeed, PCA constitutes a useful way to investigate the multivariate data as it leads to a statistical distribution of the spectral properties that can be related to the spatial distribution of the spectra. Although the relationships existing between spectral features can be expressed in absolute reflectance, scaled reflectance data emphasize the spectral shape differences versus albedo and help in gaining some insight into the main spectroscopic contributions and related mineralogical variations, relying on the established classification of lunar spectral types

[*Pieters and McCord*, 1976; *Pieters*, 1993]. Consequently, PCA is performed both in absolute and scaled reflectances, and we make use of the PCA representation to understand the mixing trends and carry out an optimal detection of the extreme spectra for their possible use as mixing model end-members.), (2) establish for each pixel within the image the logical combination of end-members from the viewpoint of the regional geological context, and (3) work sequentially with a large number of end-members in the case of a complex geological environment, each mixing combination involving, however, a limited number of components.

The advantages are that one can proceed with spectral mixture analysis, even when the total number of end-members involved exceeds the dimensionality of the multispectral observational set, and that the stability of the deconvolution relative to each considered partial combination of end-members (generally involving two to three components) is improved with respect to a simple linear unmixing considering all end-members at a time. Our model produces end-member images giving the contribution per pixel of a given end-member, whatever the considered end-member combination. This information comes along, for the sake of the interpretation, with a residual image, quantifying the quality of the mixture modeling, and with a "mask" image describing how the successive mixing iterations occur and which mixing combination applies to a given pixel. For each pixel the model is considered valid under the constraints that (1) end-member fractions sum to unity, (2) no end-member fraction is negative or superpositive (>1), (3) the residual (uncertainty) is about the noise level of the data for each spectral band considered, and (4) the spectral slope difference (deviation) between the observed and modeled spectra (scaled at 0.75 μm for the Clementine set) is <3% for each spectral ratio.

If any of the above conditions is violated, the mixing solution being tested is rejected, and the pixel is considered as unmodeled. One has then to proceed with a new geological guess. The first iteration aims at depicting the regional mixing trends expected from the geology (e.g., mare-highlands mixing or regolith surface modification by ejecta). Following iterations aim at addressing well-focused geological guesses related to crust petrology and/or stratigraphy, impact-cratering processes, and mare basalt emplacement and petrology. Generally, two to three iterations, each involving combinations of two to four end-members, are requested to deconvolve 90% or more of the pixels. Some fundamental end-members may be considered repeatedly in different mixing combinations. Unmodeled pixels are shown by the uncharted part of the mask image and represent local units not taken into account which may require specific investigations.

Coming back to the case of Reiner Gamma region, we identify at once three basic end-members relevant for modeling the observed spectral variations (see section 2.2) in the vicinity of Reiner Gamma Formation. These are mare background (MB), southwest swirl (SWS), and Reiner Gamma soil (RGS) and are derived from the previous identification of extreme spectral types (compare section 2.2). They are displayed on Plates 2m (spatial distribution) and 2q (PCA plot) using a star symbol. Any attempt involving only two end-members among these three is unsuccessful while this ternary combination models, with residuals per wavelength of the order of the noise level (i.e., 1-2%), 73% of the pixel population and well handles the regional context (see Plates 3a, 3b, and 3c and mapping in red in Plate 3f). The second iteration (Plate 3f, mapping in green) aims at describing the leftover variability associated with the unmodeled mare units and thus considers a simple binary combination of MB

with a new end-member named MHB, detected in the previous analysis (compare section 2.2) and associated with Marius Hills volcanic complex (see Plates 2m and 2q). The following iterations (iterations 3 and 4, in dark blue and yellow, respectively) deal with the leftover local lithological variability of the regolith associated with impact craters (e.g., Reiner crater and small mare craters) and consider successively a binary (MB and MC) and ternary (MB, MC, and MHB) mixture, involving a fresh mare crater end-member named MC (mare crater) (see Plates 2m and 2q). Accordingly, with the four successive iterations described above, the image variance can be explained, with the following respective cumulative proportion of pixel population: 73, 88, 92, and 96% (unmodeled parts of the image remain in white in Plate 3f). Plate 3g gives the distribution of the root-mean-square residual and thus provides us with a control on the relevance of the linear deconvolution. One sees that the residuals are <2% rms, with the major part of the scene modeled at the 1% level or better.

3. Interpretation

The fractional abundance images associated with RGS, MB, SWS, MHB, and MC end-members are shown in Plates 3a, 3b, 3c, 3d, and 3e, respectively, and provide valuable information in terms of spatial distribution. The RGS contribution (Plate 3a) appears to be restricted to RGF and the northeastern elongated high-albedo pattern, located northeast of RGF. The MB contribution is very homogeneous in the regional mare area (coded in red in Plate 3b), with, however, local variations mainly seen around and southwest of RGF and additional localized patches associated, for instance, with Reiner crater. These variations result from a variable mixing between MB and SWS, with respective proportions typically ranging between 60-80% and 40-20% (Plates 3b and 3c). The MHB contribution correlates very conspicuously with the south part of the Marius Hills volcanic complex (Plate 3d). The MC contribution is quite localized and mainly describes the distribution of the fresh mare impact craters piercing the regolith layer (Plate 3e). As mentioned in section 2.3, the end-member combination used for a given pixel to establish the relative end-member contributions is indicated in Plate 3f.

It appears that the surface material variability observed in the Reiner Gamma region can be depicted with three components. The first two components exhibit spectral characteristics consistent with a prevailing contribution of mature mare soils for the surroundings (MB) and of immature mare crater-like soils (RGS) at RGF. The third intermediate-albedo component (SWS) has general characteristics of a mature mare soil, but with a redder continuum slope. In basic agreement with the first multispectral imaging surveys, which were, however, less documented [Johnson et al., 1977; Bell and Hawke, 1981], the regional distribution revealed in this work by the spectral mixture analysis shows the existence of a diffuse triangle-shaped unit (coded in green and yellow in Plate 3c) surrounding RGF in its immediate vicinity. It corresponds very exactly to the enigmatic medium-albedo unit (see section 2.1 and Figure 2i), detected from its low 0.40/0.56 μm contrast ratio [Bell and Hawke, 1981] and referred to as the red halo unit in the literature. The SWS contribution, needed to describe the modified spectral signature of the mare in the red halo area, appears to be quite prevailing in a few patches southwest of Reiner Gamma Formation (Plate 3c), where the end-member SWS is picked up from the PC's statistical analysis (see Plates 2m-2q). In the red halo the SWS contribution is ~30%, and given the 3-4% slope difference in the UV-VIS domain between the MB and SWS

end-member spectra (Plate 2o), it explains why the red halo multispectral observation was so subtly different from that of the surroundings [Bell and Hawke, 1987].

In Plates 4a and 4b, MHB and SWS fraction images are overlain onto the high-resolution Lunar Orbiter frame to emphasize the relationships with the detailed morphology. The red-yellow-coded unit seen in the north in Plate 3d is clearly related to morphological units belonging to the Marius Hills volcanic complex. Spectra (Plates 2n and 2o) indicate very low albedo terrains, high UV/VIS ratios in the range 1.09-1.10, concave-down inflection in the near-infrared, and thus very weak absorptions at 1.0 μm and are consistent with very mature high-titanium mare basalt soils. These spectra characteristics at high spatial resolution are quite consistent with earlier telescopic observations made at Marius Hills [Pieters and McCord, 1976] and more recently from Galileo imaging data, reporting the presence of a mhW mare basalt type [Sunshine et al., 1994], and from an independent analysis of Clementine data covering the Marius Hills volcanic complex [Weitz and Head, 1999]. Interestingly, local distributions are also detected in association with Reiner crater ejecta and with the dark mare unit south of Reiner Gamma Formation. It suggests that this mhW mare basalt unit predates the emplacement of the regional MB mare basalt unit.

The results above show that the surface layer of the regolith at RGF (class 3 in Plate 2) has specific characteristics. It comprises very immature soils and presents an increase of its iron content (13.5-14.5 wt%) with respect to the surrounding background surface, as described in class 1 (11-12.5 wt%). The overall optical and spectroscopic properties of the regolith present at RGF and characterized by the RGS end-member (see Plates 2n and 2o) are those of immature small mare crater-like soils [McEwen et al., 1993], caused by the ejecta excavating and redistributing subsurface mare regolith. Despite the fact that, as assessed from the telescopic multispectral survey (section 2.2.1), the spectral analysis is not consistent with a regional contamination from large impact craters such as Cavalerius, we seek to test and constrain the idea that the regolith at RGF could have optical properties close to those of shallow subsurface mare material [Bell and Hawke, 1981]. From studies investigating the regolith layering and stratigraphy on the basis of lunar core samples [McKay et al., 1991] there is a general consensus that grain size variations occur with depth. Although not systematic, the observed trend suggests that there is a general increase in the mean grain size and in the degree of immaturity with depth.

Building upon experimental results produced by laboratory spectroscopic analyses of sieved size separates of lunar soils from Luna-16, Luna-20, and Luna-24 sites [Antipova-Karataeva et al., 1979; Pieters et al., 1993; Starukhina and Shkuratov, 1996] and inferences drawn by Bell and Hawke [1981], we show hereafter that one can explain the reported RGS-SWS spectral behaviors by a mechanism which would mainly remove the finest fraction in the soil (particle diameter < 45 μm) at RGF and redistribute it in the vicinity with a laterally variable proportion and local accumulations such as at the SWS site. This mechanism would be responsible for the disruption at RGF of the optical characteristics of mature soils, caused by the natural space-weathering effects.

First of all, it is shown in Figure 3 that the RGS-type spectral characteristics are very close to those of the Luna-24 spectrum (produced from sample 24085 collected at 85-86 cm depth of the Luna-24 core) [Pieters et al., 1993] and correspond to separates with size ranging between 45 and 94 μm, i.e. the size range for which the spectral contrast is maximum.
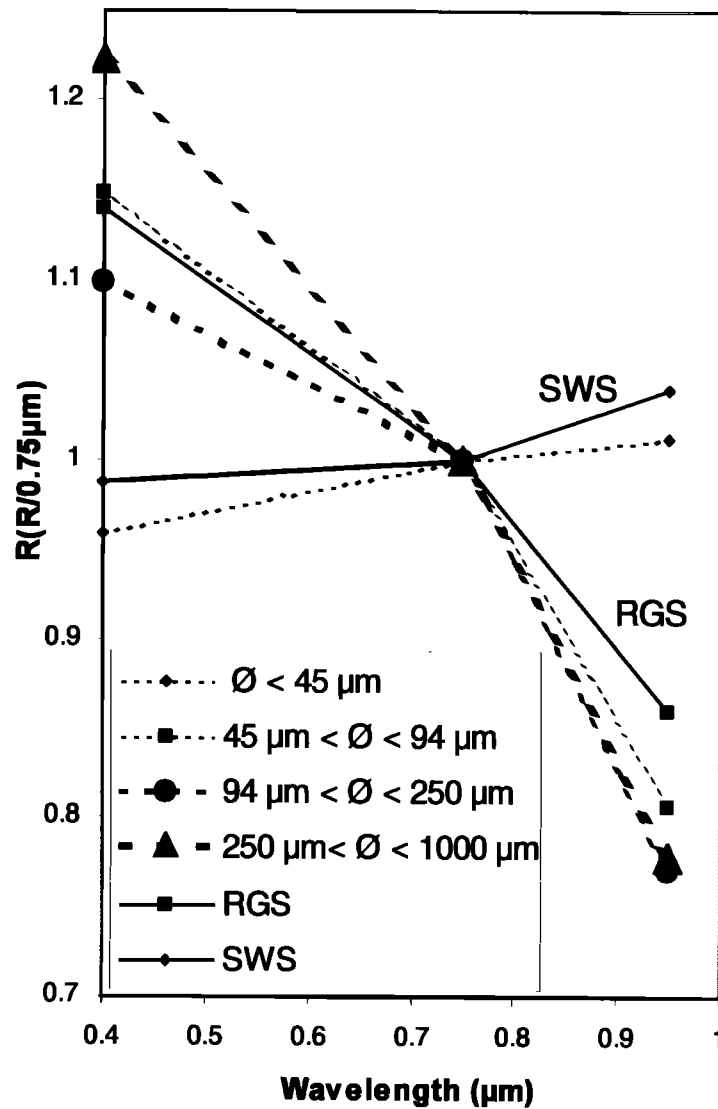
Figure 3. Interpretation of RGS and SWS spectral data on the basis of Luna-24 (sub)mature mare soil laboratory spectra produced for different size fractions (<45 μm, 45-94 μm, 94-250 μm, and 250-1000 μm) and normalized to the bulk soil spectrum. The reflectance spectra are taken from *Pieters et al.* [1993] and were produced from the sample 24085, obtained from horizon 85-86 cm of the Luna-24 core. $R = \{B(\lambda)/B_0(\lambda)\}/\{B(0.75 \mu m)/B_0(0.75 \mu m)\}$, where $B_0(\lambda)$ is the bulk soil reflectance at wavelength λ and $B(\lambda)$ is the separate fraction reflectance at wavelength λ. The fine fraction has a significant influence on the red slope continuum in the 0.4-0.75 μm range and on the absorption depth in the 0.75-1 μm range. The RGS characteristics are well matched by the 45-94 μm size fraction spectrum while SWS behavior is close to the fine fraction spectrum.

Second, we investigate the iron content variation in the regolith as a function of depth and size fraction range. For this matter, we consider the Luna-24 and Apollo 17 sites for which well-documented cores by means of chemical analyses do exist (*Barsukov et al.*, [1980]; cores 70001-70009, *Papike et al.* [1982]). The chemical analyses show that the Luna 24-soils and Apollo 17 mare basalts have an FeO content in the same range, 21 and 19 wt % (i.e., 16.3 and 14.8 wt% iron content), respectively (see Table A8.1 of *Haskin and Warren* [1991]). In both cases, the same trend, the iron content increasing with depth for the largest size fractions, is noted. For the Luna 24-site, *Barsukov et al.* [1980] have found that the FeO content at a depth ranging from 0.3 to 1.0 m is 16.0-16.3 wt% (i.e., 12.5 wt% iron content) for the fine fraction (<74 μm) while the FeO content of the bulk, at the same depth, is 18.8-20 wt% (i.e., 14.5-15.5 wt% iron content). At

the Apollo 17 site [*Papike et al.*, 1982] we note that the iron-rich phase (ilmenite basalt) predominates in the range of the size fractions comprised between 20 and 90 μm and for the largest size fractions. Furthermore, variations occur with depth such that between 0.3 and 0.8 m below the surface the proportion of the iron-rich phase increases up to 60% for the 20-90 μm size fractions and 80% for the largest ones, while for the upper 20 cm layer it amounts only to 45 - 55%. These different observations could explain the local variation seen in the iron content between class 1 and class 3 (see Plate 2 and section 2.2.2.2), ranging from 12 wt% in the mare surroundings to 14 wt% at RGF and occurring in relation to a possible stripping of the uppermost layer inducing a modification of the size fraction proportion.

Third, in the same range of depth (below 0.2-0.3 m) of the Apollo 17 drill core the soil average maturity index I_s/FeO is ~10-
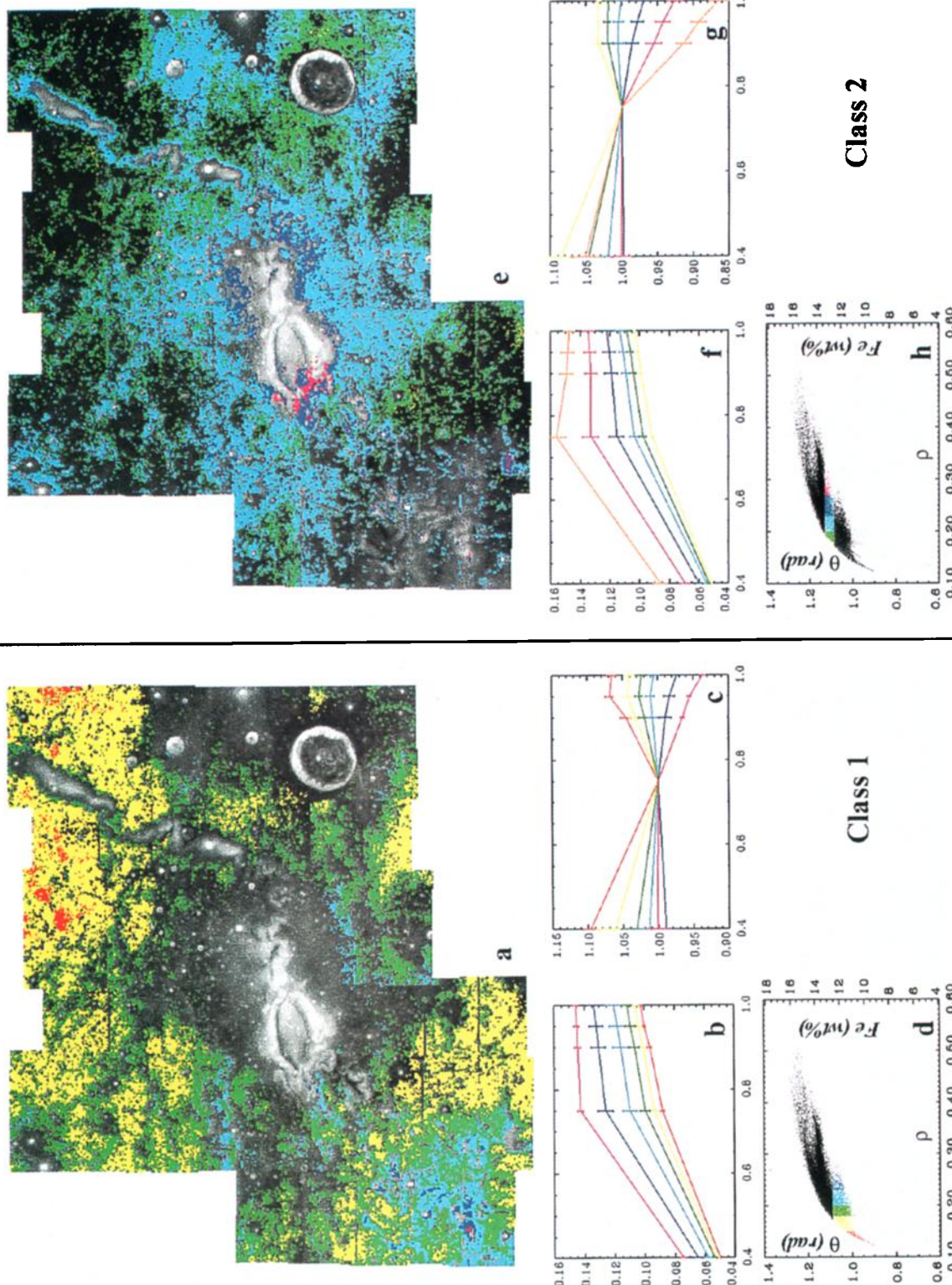
Plate 2. Iron content and soil maturity variations across the Clementine mosaic according to *Lucey et al.'s* [1995] approach. (Plates 2a-d, 2e-h, and 2i-l) For given iron content classes, soil maturity variations ranging from mature (coded in red, yellow, and green) to submature (light blue and dark blue) and immature (pink, orange, dark green) soils. For each class are given the location of the considered boxes in the (ρ (soil maturity parameter), θ (iron content parameter)) space (Plates 2d, 2h, 2l), the associated spatial distributions (Plates 2a, 2e, 2i), and the corresponding average spectra in reflectance and relative to MS2, scaled at 0.75 μm (Plates 2b, 2c, 2f, 2g, 2j, 2k). (Plates 2m-q) Representation of the most extreme spectral types derived from the present analysis and marked by stars. For each spectral type (Plates 2n, 2o), the location of the related box in the (ρ, θ) space (Plate 2p), in the PCA cloud derived from the UV-VIS Clementine image cube and projected along its first and second principal axes (Plate 2q), and the associated spatial distribution (Plate 2m) are shown.
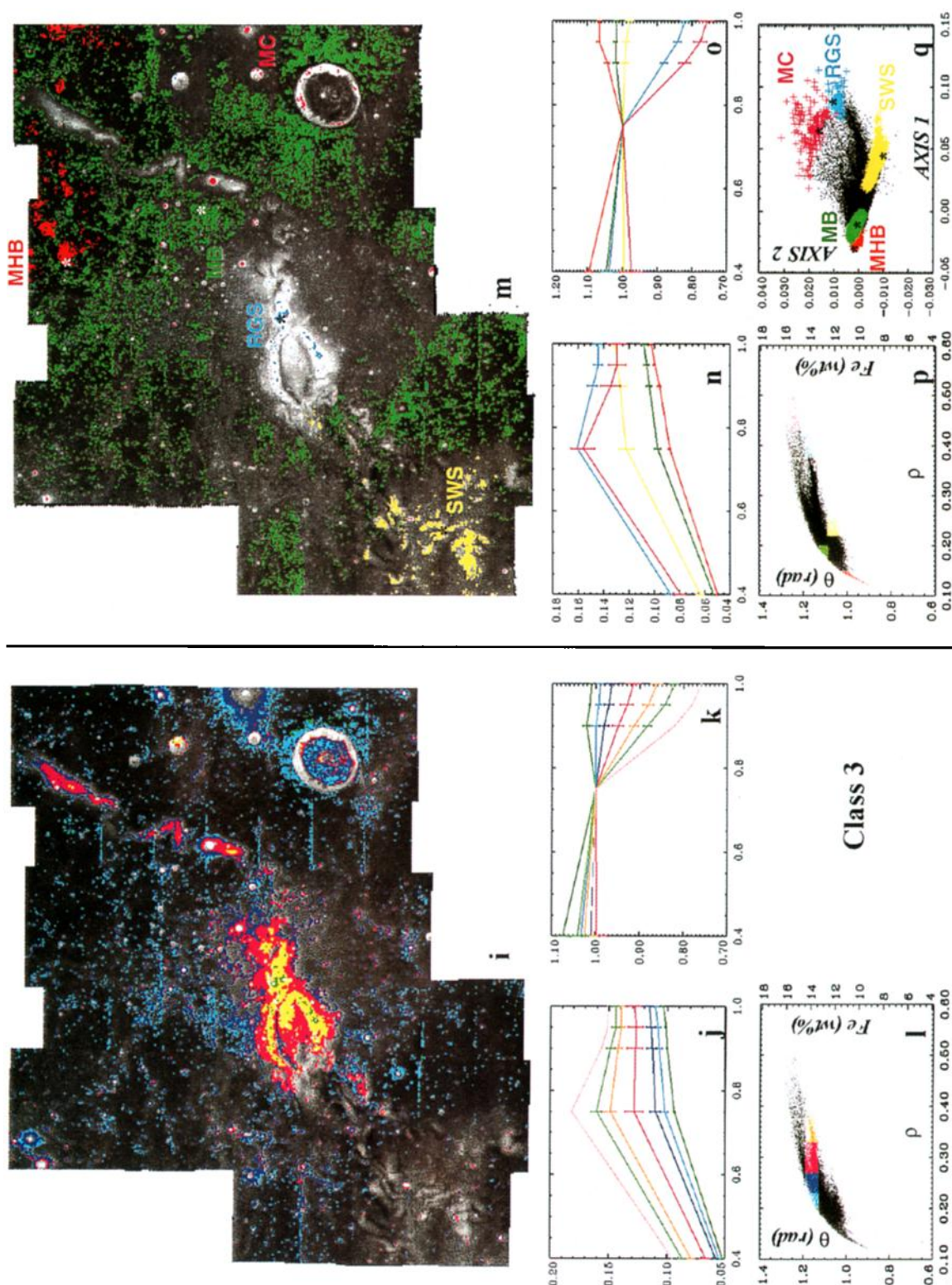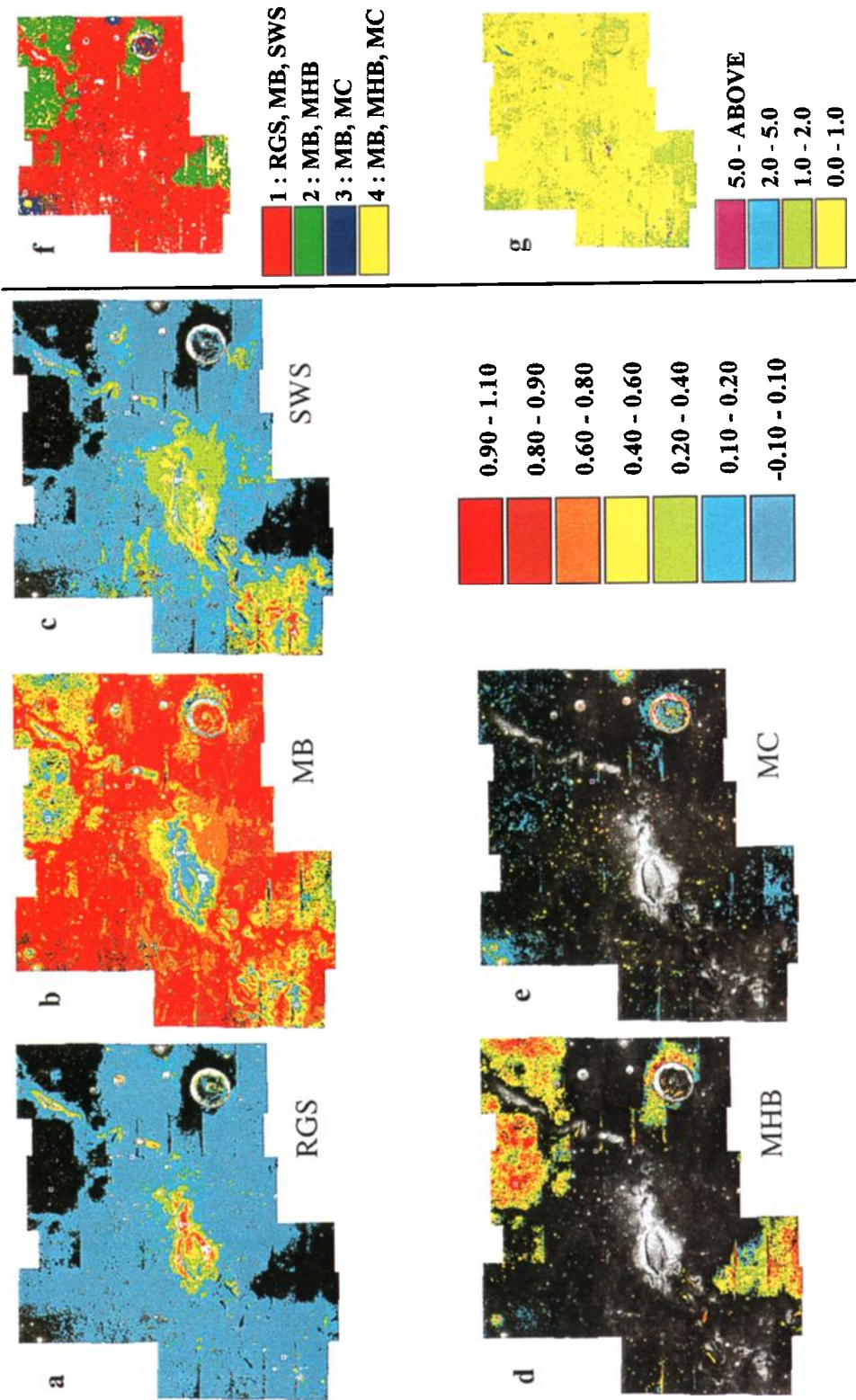
Plate 2. (continued)

Plate 3. Iterative spectral mixture modeling using five regional end-members. Plates 3a, 3b, 3c, 3d, and 3e correspond, whatever the considered mixture combination (see below with Plate 3f), to fractional abundance images associated with end-members RGS (Reiner Gamma Formation soil), MB (regional mare basalt background soil), SWS (southwest swirl soil), MHB (Marius Hills basalt), and MC (fresh mare impact crater), respectively. Color coding for fractional abundance f is as follows: dark blue, $-0.1 < f < 0.1$; light blue, $0.1 - 0.2$; green, $0.2 - 0.4$; yellow, $0.4 - 0.6$; orange, $0.6 - 0.8$; brown, $0.8 - 0.9$; and red $0.9 - 1.1$. Plate 3f shows the iterative steps of the mixture modeling: Mapping in red corresponds to the first mixing, combining RGS, MB, and SWS; mapping in green indicates the extent modeled as a combination of MB and MHB; mapping in dark blue indicates a combination of MB and MC; mapping in yellow refers to a MB, MHB, and MC combination. Plate 3g is a mean residual image showing the quality of the spectral modeling for each pixel. Residuals are expressed in % rms and color coding is as follows: yellow, <1%; green, >1% and <2%; blue, > 2% and <5%; and magenta, >5%.
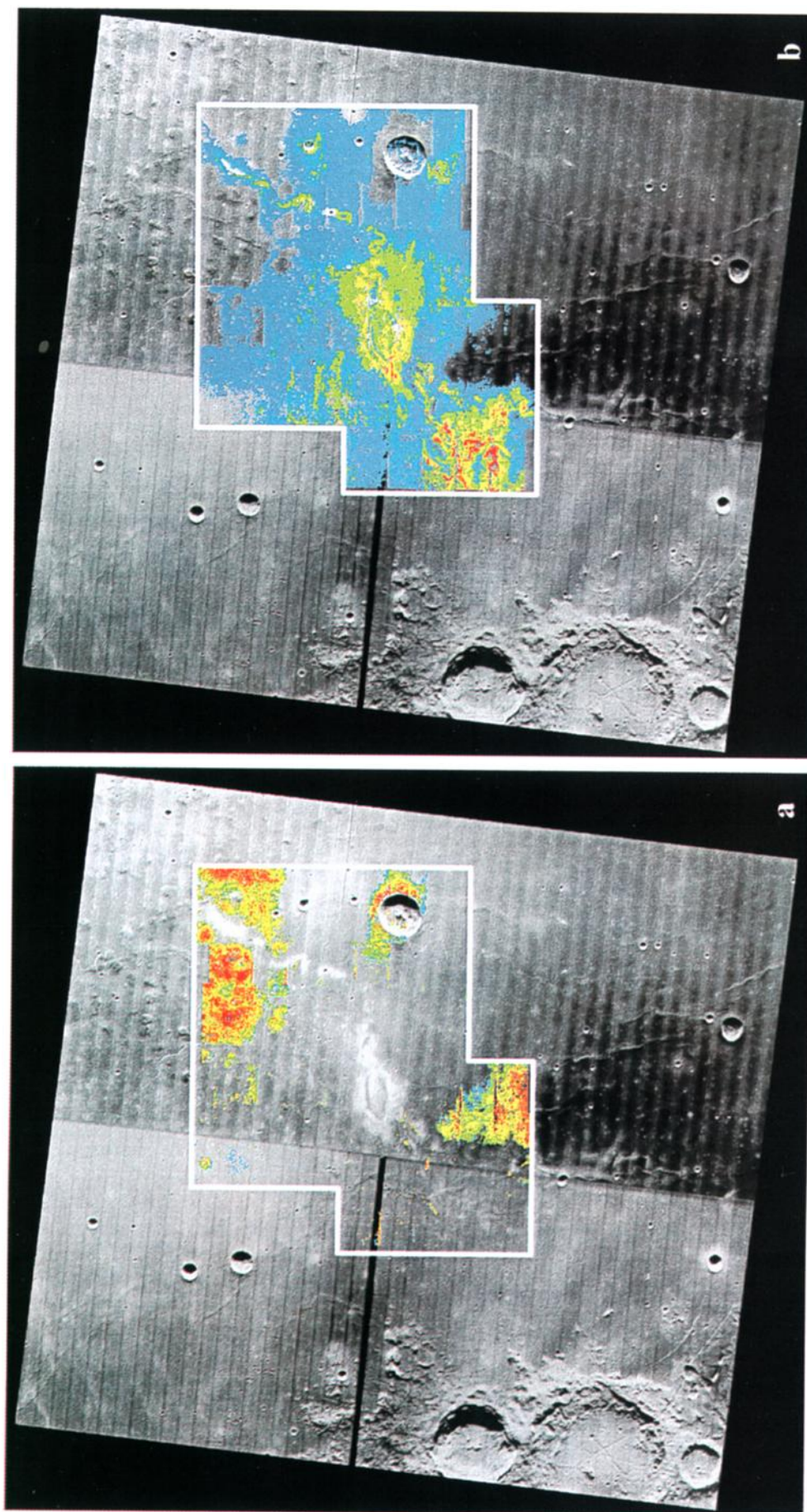
Plate 4. (a) MHB fraction image overlain onto Lunar Orbiter IV image (IV-157 and IV-162). The red-yellow-coded unit is clearly related to morphological units belonging to Marius Hills volcanic complex. Spectra indicate very low albedo terrains, high UV/VIS ratios in the range 1.09-1.10, concave-down inflection in the near-infrared, and thus very weak absorptions at 1.0 μm and are consistent with very mature high-titanium mare basalt soils. These spectra characteristics at high spatial resolution are quite consistent with earlier telescopic observations made at Marius Hills [*Pieters and McCord*, 1976] and more recently from Galileo imaging data, reporting the presence of a mhW mare basalt type [*Sunshine et al.*, 1994]. Interestingly, local distributions are detected in association with Reiner crater ejecta and with the dark mare unit south of Reiner Gamma Formation. (b) SWS fraction image overlain onto Lunar Orbiter IV image (IV-157 and IV-162). The spectral mixture analysis reveals the existence of a diffuse triangle-shaped unit (coded in green and yellow) surrounding RGF in its immediate vicinity. It corresponds very exactly to the enigmatic medium-albedo unit (see section 2.1 and Figure 2i), detected from its relatively low 0.40/0.56 μm contrast ratio [*Bell and Hawke*, 1981] and referred to as red halo unit in the literature. The SWS contribution, needed to describe the modified spectral signature of the mare in the red halo area, appears to be quite prevalent in a few patches south of Reiner Gamma Formation, where the end-member SWS was picked up.

20 (see Figure 7.26 of *McKay et al.* [1991, p. 336]). In the case of the Luna-24 core the observed particle track records indicate a higher degree of maturity for the upper zone of the regolith column, as compared to the soil index in the lower zone [*Goswami et al.*, 1979]. Correlatively, the average maturity index I_s/FeO decreases from ~40 at a shallow subsurface level of 0.2 m depth to 25 at a 1.0 m depth [*Morris*, 1978]. It is consistent with our mapping detecting locally within RGF the occurrence of very immature regolithic soils referred to as class 3, in sharp contrast with the surrounding surface material belonging to class 1 (see Plate 2).

According to the above-mentioned available in situ data documenting variations in the chemical composition, in the distribution of particle types and sizes, and in the degree of maturity with depth in the lunar mare regolith, the characteristics reported for the RGF regolith are consistent with the properties of a subsurface soil layer from a depth of the order of 0.3 – 0.8 m. This agrees with the inference of *Bell and Hawke* [1981, p.693], that "the agglutinate-rich surface layer on the original regolith must have been removed to a depth of 10-20 cm".

Conversely, the SWS-type characteristics are rather consistent with an accumulation of the finest fraction which dominates the optical properties of the mare soil and is responsible for the spectrum reddening [*Hapke*, 1981; *Pieters et al.*, 1993; *Mustard and Hays*, 1997]. Its perfect MS2-like spectral shape (Plate 2o), the associated estimates ranging for the ρ maturity parameter between 0.22 and 0.25, corresponding at first order to an I_s/FeO estimate above 70 [*Pinet et al.*, 1997] and for the iron content between 11.5 and 12.5 wt% (Plate 2p), are characteristic of a rather mature mare regolith. The fact that within class 1 (Plate 2d), the SWS-like material exhibits the highest ρ value arises from the very high titanium-rich composition of the dark MHB material which it is basically compared to (see Plates 2a and 3d).

Lucey et al.'s [1995] proposed method may also present some limitations in this case [*Lucey et al.*, 1998; *Jolliff*, 1999], and the relative difference on the parameter ρ estimates may not mean a significant difference in maturity. However, the intermediate albedo of SWS spectrum (1-2% higher than MS2 spectrum) suggests that whatever process disturbed the surface to form the main RGF feature also indirectly disturbed the surface to a lesser extent in the SWS area. The proposed mechanism of redeposition of the finest fraction may have been, for instance, accompanied by a process involving an optical modification of the surface resulting in a slight albedo increase and maturity change. The relatively low iron content may also reflect a lateral increase in the proportion of highlands debris contaminating the mare regolith when approaching the edges of Oceanus Procellarum [*Mustard and Head*, 1996].

RGS and SWS fraction images (Plates 3a and 3c) and related Plate 4b exhibit that there is a certain level of spatial organization in both RGS and SWS distributions. Indeed, if one considers an end-member relative abundance higher than 50-60%, the RGS end-member distribution appears to be very focused within a circle of 30 km diameter, centered on the northeastern part of RGF, with some local additional rather linear patches located northeast of the formation. The main concentration appears to be spatially correlated with the magnetic anomaly detected from the Apollo 15 and 16 subsatellite magnetometer data [*Hood et al.*, 1981]. The northeastern patches detected from the mixture analysis [*Pinet et al.*, 1998] suggested the occurrence of an additional magnetic anomaly, which has been mapped quite recently by Lunar Prospector [*Hood et al.*, 1999]. Conversely, the distribution and proportion of the SWS end-member are maximal

at the southwesternmost part of Reiner Gamma and display a regional concentration, located southwest of the formation within a distance of 50-60 km, with diffuse patches in the surroundings, associated with observed swirl-like patterns and clusters of small-sized craters <1 km in diameter, having characteristics such as very shallow and smoothed morphological features (see Lunar Orbiter frame IV-157). It is presently impossible to determine whether the optical diffuse swirl-like pattern is independent from the emplacement of old Cavalerius secondaries, but given the results above, it would be worthwhile to examine this option. Higher-resolution (10-30 m) images are clearly needed to further investigate in this matter. The detailed examination (Plates 1f-1i, 2e-2h, 2i-2l, and 3e) does not point at any particular impact crater or cluster of craters as a potential source of ejecta material accounting for the optical and spectroscopic properties seen at RGF (see further in the text). However, in our view, the different pieces of information gained from the present study, (1) optical and mechanical modification of the uppermost layer of the regolith unrelated to compositional/lithological variations caused by the regional geological context, (2) prevailing northeastern-southwestern orientation and 100 km scale of the observed distribution, (3) very limited morphological features including, however, swirls and clusters of small shallow craters, and (4) spatial correlation with the detected magnetic anomalies could be reasonably pieced together in the hypothesis of a responsible mechanism involving the fall of fragments of a low-density (of the order of 0.3 g/cm^3) cometary nucleus [*O'Keefe and Ahrens*, 1982; *Schenk et al.*, 1996; *Meech*, 1996], previously disrupted by tidal interaction in the Earth-Moon system. Simulations of the process of tidal disintegration for the comet Shoemaker-Levy 9 have shown that the resulting cloud of debris comprises small-sized fragments in the range of a few centimeters to meters in scale [*Rettig et al.*, 1996]. Following current estimates of 5-20 km/s for cometary impact velocities [*Schultz and Snrka*, 1980; *O'Keefe and Ahrens*, 1982], 10 and 25 km/s velocities are considered in a preliminary calculation [*Shevchenko*, 1997] based on *Melosh* [1989] which shows that the maximum diameter for the impacting fragments should not exceed 40 m (respectively, 25 m) if the mean density of the ice impactor is ~1.0 g/cm^3. Assuming that the tidal disruption occurs within 4 Earth radii from the Earth and taking 1m/s for the velocity dispersion of the fragments within the resulting cloud yields one an impact on the lunar surface taking place ~12 hours later, with an elongated cylinder-shaped cloud having a typical size of 80-90 km (respectively, 30 km for a 25 km/s velocity range), consistent with the spatial scale of the surface optical modifications associated with Reiner Gamma features. Given the low density of these fragments (0.3 g/cm^3 or possibly less), the effects of impacts on the lunar surface may be quite different from those caused by a high-density body with tensile strength close to that of the lunar surface. It is anticipated that these bodies might not generate true craters in the lunar regolith, but only shallow flat-bottomed ones [*O'Keefe and Ahrens*, 1982; *Frank et al.*, 1986]. In such a case, these features are still beyond the reach of the present observations, and their detection waits for a detailed geomorphological survey of the area. The observed crater concentration in the RGF area suggests that in the case of an impactor density of 0.1 g/cm^3 [*O'Keefe and Ahrens*, 1982] the largest diameter for the impacting fragments would not exceed ~0.6 km, and the possible parent body (cometary nucleus) diameter would be ~3 - 4 km.

The different observations put together in the present paper are consistent with the idea that in the area of RGF the upper layer of the regolith could have been optically modified and stripped off

down to a depth of 0.5-1 m. The overall distribution noted from RGS and SWS end-member fraction images suggests that the incidence angle of the conjectured impacting body should have been rather pronounced in order to account for the distance of separation of the order of 100-120 km between the locations of RGS and SWS end-member maximal concentrations. In such a view (Figure 4) the near-surface regolith layer in RGS areas was modified by the oblique "impact" of a low-density impactor of cometary type, surrounded by a dust-gas coma, which moved from the northeast direction and interacted with the lunar surface under a high incidence angle. On the basis of calculations made by O'Keefe and Ahrens [1982], in the case of a very low density impactor (cometary nuclei described as a snowball or a particle swarm) the average of the excavation depth is near zero, and the vapor cloud produced by hypervelocity impact moves nearly along the surface, carrying away preferentially the fine fraction of the soil. The selective transportation of the fine fraction (<45 µm) over regional distances and in a specific northeastern-

southwestern direction could be the result of a wind-like-type event. This would be redeposited at a distance of ~100 km from the RGS site and would be responsible for the observed concentrations, seen in the southwest swirl patterns. The surface regolith could have been then optically modified by the redeposition dynamical process, resulting locally in a slight albedo increase (1-2%) and a weak relative immaturity effect.

An alternative scenario [Hood et al., 1979; L.L. Hood, personal communication, 1999] would be that the cluster of small craters located at the westernmost tip of the RGF main swirl is indicative of a low-angle impact coming from the west. In that case these craters would be the source of ejecta material distributed on the surface within the main swirl. Though a definitive answer cannot be provided, we do not favor this possibility as, according to our results, the maximal effect of interaction and modification of the regolith is centered on the northeastern part of RGF (Plates 2i-2l and 3a, and Figure 4). Indeed, the progressive decrease in iron content seen in Plate 2
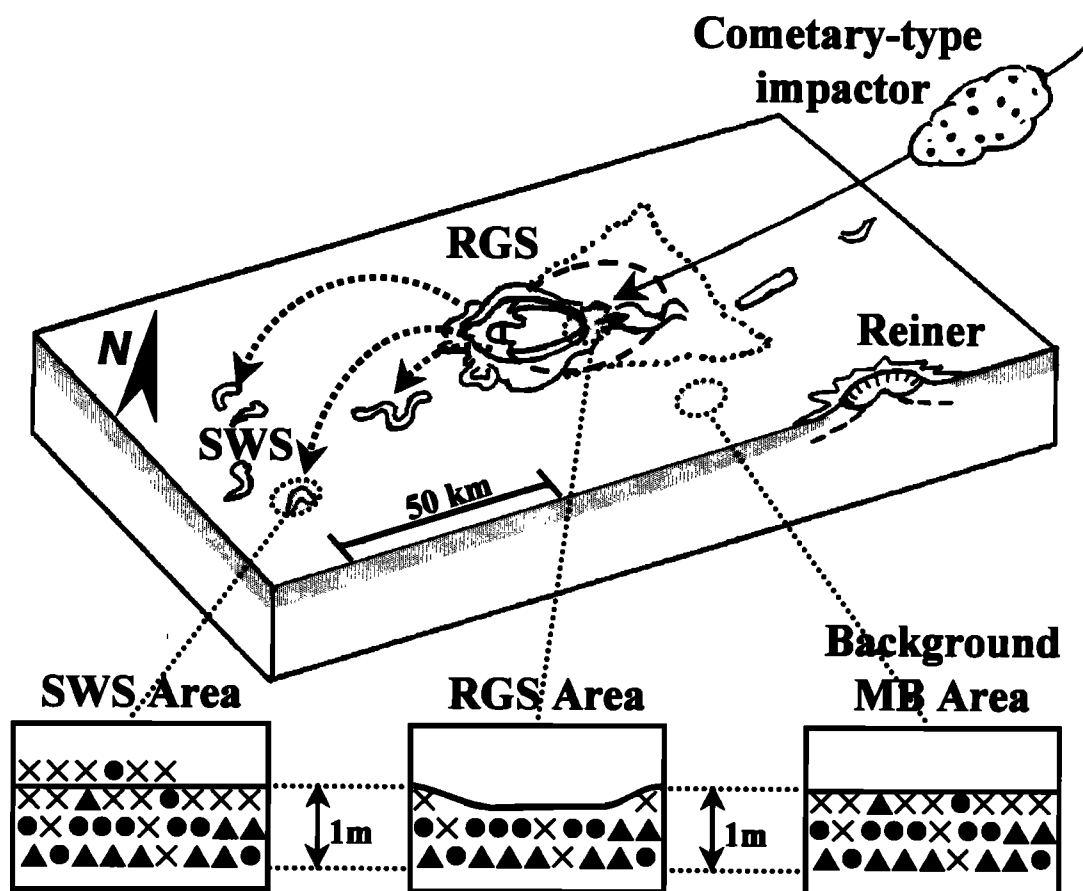

Figure 4. Sketch of the disturbing effects in the regolithic near-surface layer (depth of the order of 1 m) caused by an oblique impact of a cometary low-density body and accounting for the observed optical modifications. Shown is the upper layer of the typical mare soil: crosses refer to the fine fraction of the mare soil with diameter $\emptyset < 45$ µm; solid circles refer to the size fraction with $45 < \emptyset < 94$ µm; and solid triangles refer to the coarse size fraction >95 µm. Physical characteristics (size fraction distribution and modification of the soil layering) of the regolith layer at the RGS, SWS, and MB sites are sketched in the corresponding cross sections. MB refers to the undisturbed mare background situation; RGS corresponds to a relative depletion of the fine fraction and correlative enrichment of the 45-94 µm size fraction; and SWS shows a relative fine fraction enrichment by the deposition of the fine fraction transported by a wind-like-type effect (see text). Dashed circle indicates the extent of the zone where the fine fraction is prevalently removed, as typified by RGS end-member and related cross section. Dotted triangular contour demarcates the extent of the zone where the mare regolith is modified. It corresponds spatially to the red halo unit (see Figure 2i), modeled by a combination of 20-40% of the SWS end-member mixed with 60-80% of the MB end-member (see Plates 3b and 3c).

from classes 3 to 1 reveals that RGS (class 3), representative of most of the RGF surface unit, is closer to the MC end-member, which is characteristic of a pure mare basalt excavated from some depth, than the class 2 material (coded in pink and dark blue in Plates 2e-2h) associated with the cluster of small craters at the RGF westernmost tip with a V-shaped albedo pattern to the east, which appears both peripheral to RGF and is more shallow than RGS. It suggests that these small craters are secondary effects of the Reiner Gamma event.

The observed magnetic properties at Reiner Gamma Formation could then be explained by inductive effects occurring during the impact, or, more precisely, the interaction between the lunar surface and the cometary environment, as proposed by *Schultz and Snrka* [1980]. Indeed, collisions of small comets, with their ionized gaseous envelopes, are capable of impressing local patterns of magnetization [*Gold and Soter*, 1976]. The ambient solar wind magnetic field is briefly but strongly enhanced as the large partially ionized cometary atmosphere is compressed against the planetary surface. The shock produced by collision of the comet solid fragments occurs at the time of this field enhancement, resulting in local shock magnetization and possible subsequent solar wind ion deflection contributing to the unusual optical properties observed at RGF as proposed by *Hood and Williams* [1989].

4. Conclusions

The findings of the present paper evidence that three components in terms of surface material are present in the region of the Reiner Gamma Formation (RGF). The first two components exhibit spectral characteristics consistent with a prevailing contribution of mature mare soils for the surroundings (MB) and of immature mare crater-like soils (RGS) at RGF, incorporating a small proportion of highlands debris or fragments mixed in the subsurface layer of the mare regolith as seen by *Bell and Hawke* [1987]. The third intermediate-albedo component (SWS) has general characteristics of a mature mare soil, but with a redder continuum slope. Paradoxically, the SWS material presents a slight increase in albedo, resulting in a second-order relative immaturity effect. Its relative lower iron content estimate may reflect a lateral increase in the proportion of highlands debris contaminating the mare regolith when approaching the edges of Oceanus Procellarum.

The regolithic surface layer at RGF has clearly unusual specific characteristics. The overall optical and spectroscopic properties of the regolith characterized by the RGS end-member are close to those of immature small mare crater-like soils and reflect an increase in the iron content (13.5-14.5 wt%) with respect to the surrounding background surface (11-12.5 wt%). According to the limited available set of in situ data documenting variations in the chemical composition, in the distribution of particle types and sizes, and in the degree of maturity with depth in the lunar mare regolith those characteristics are consistent with the properties of a mare subsurface soil layer from a depth of the order of 0.3 − 0.8 m, comprising a small highland component, differing from the MC mare crater end-member, which exhibits a higher iron content (15-16 wt%) characteristic of a pure mare basalt. The optical and mechanical properties are also consistent with thermodynamical and mechanical considerations derived from impact-cratering theoretical works and support the hypothesis that the uppermost part of the regolith could have been modified through an interaction involving the fall of fragments of a low-density cometary nucleus, previously broken by tidal disruption in the

Earth-Moon system. The Reiner Gamma magnetic anomaly would then not be the result of an antipodal crustal field generated by the large impact crater and basin formation process, but would rather arise from local inductive effects occurring during the interaction between the lunar surface and the cometary environment, with the possibility that subsequent solar wind ion deflection takes place and contributes to the persistence of the unusual optical properties.

Though we consider the proposed scenario to be, in the line of the principle of Occam's razor, the simplest way to account for the whole body of information today available, we recognize, however, that in the present state of knowledge, one cannot rule out the hypothesized existence of a zone of seismically modified terrain peripheral to the Imbrium or Orientale basins just beneath the mare surface that would be the actual source of the RGF magnetic anomaly. In this view the RGF albedo marking would result from the emplacement of secondary crater ejecta excavated from shallow depths beneath the preexisting mare surface, this material having been both exposed much more recently than that composing the impact basins ejecta and selectively shielded from the solar wind ion bombardment.

In any event, the RGF case suggests that additional areas may exist on the Moon where the regolith could present locally unusual optical, mechanical, and magnetic properties, requiring for their detection from orbit a detailed high-resolution survey of the lunar surface such as the one performed by the low-altitude Lunar Prospector mission or the ones to come with Smart-1, Lunar-A and SELENE missions.

References

Adams, J. B., M.O. Smith, and P.E. Johnson, Spectral Mixture modeling: A new analysis of rock and soil types at the Viking Lander 1 site, *J. Geophys. Res.*, *91* (B8), 8098-8112, 1986.

Antipova-Karataeva, I I., et al., Optical parameters of regolith from mare and highland regions of the Moon, in *Soil From Highland Region of the Moon* (in Russian), pp. 585-588, Nauka, Moscow, 1979.

Barsukov, V.L., L.V. Dmitriev, L.S. Tarasov, G.M. Kolesov, I.D. Shevaleevskii, G.I. Ramendik, and A.V. Garanin, Geochemical and petrochemical characteristics of regolith and rocks from Mare Crisium (preliminary data), in *Lunar Soil From Mare Crisium* (in Russian), pp. 158-165, Nauka, Moscow, 1980.

Bell, J.F., and B.R. Hawke, The Reiner Gamma Formation: Composition and origin as derived from remote sensing observations, *Proc. Lunar Planet. Sci. Conf.*, *12th*, 679-694, 1981.

Bell, J.F., and B R. Hawke, Recent comet impacts on the Moon: The evidence from remote-sensing studies, *Publ. Astron. Soc. Pac.*, *99*, 862-867, 1987.

Blewett, D.T., P.G. Lucey, B.R. Hawke, and B.L. Jolliff, Clementine images of the lunar sample-return stations: Refinement of FeO and TiO$_2$ mapping techniques, *J. Geophys. Res.*, *102* (E7), 16,319-16,325, 1997.

Boardman, J.W., Automating spectral unmixing of Aviris data using convex geometry concepts, *JPL Publ.*, 93-26, 11-14, 1993.

Chevrel, S.D., and P.C. Pinet, Revisited geology of Gassendi crater from Earth-based near-infrared multispectral solid state imaging, *Proc. Lunar Planet. Sci.*, *22nd*, 249-258, 1992.

Chevrel, S.D., P.C. Pinet, and J.W. Head, Gruithuisen domes region: A candidate for an extended nonmare volcanism unit on the Moon, *J. Geophys. Res.*, *104*, 16,515-16,529, 1999.

Cloutis, E.A., Hyperspectral geological remote sensing: Evaluation of analytical techniques, *Int. J. Remote Sens.*, *17* (12), 2215-2242, 1996

Fisher, E. M., and C.M. Pieters, Remote determination of exposure degree and iron concentration of lunar soils using VIS-NIR spectroscopic methods, *Icarus*, *111*, 475-488, 1994.

Fisher, E.M., and C.M. Pieters, Composition and exposure age of the Apollo 16 Cayley and Descartes regions from Clementine data Normalizing the optical effects of space weathering, *J. Geophys. Res.*, *101* (E1), 2225-2234, 1996.

Frank, L.A., J.B. Sigwarth, and J.D. Craven, Reply, *Geophys. Res. Lett. 13* (11), 1186-1189, 1986.

Gaddis, L.R., A.S. McEwen, and T.L. Becker, Compositional variations on the Moon/ recalibration of Galileo solid-state imaging data for the Orientale region and farside, *J. Geophys. Res.*, *100* (E12), 26,345-26,355, 1995.

Gold, T., and S. Soter, Cometary impact and the magnetization of the Moon, *Planet. Space Sci.*, *24*, 45-54, 1976.

Goswami, J.N., D. Lal, M.N. Rao, and T.R. Venkatesan, Depositional history of Luna 24 drill core soil samples, *Earth Planet. Sci. Lett.*, *44*, 325-334, 1979.

Hapke, B., Bidirectional reflectance spectroscopy, 1, Theory, *J. Geophys Res.*, *86*, 3039-3054, 1981.

Haskin, L., and P. Warren, Lunar chemistry, in *Lunar Sourcebook*, edited by G. Heiken, D. Vaniman, and B.M. French, chap. 8, pp. 357-474, Cambridge Univ. Press, New York, 1991.

Head, J.W., S. Murchie, J.F. Mustard, C.M. Pieters, G. Neukum, A. McEwen, R Greeley, E. Nagel, and M.J.S. Belton, Lunar impact basins: New data for the western and farside (Orientale and South Pole Aitken Basins) from the first Galileo flyby, *J. Geophys. Res.*, *98* (E9), 17,149-17,181, 1993.

Hood, L L., Magnetic field and remanent magnetization effects of basin-forming impacts on the Moon, *Geophys. Res. Lett.*, *14* (8), 844-847, 1987.

Hood, L.L., and Z. Huang, Formation of magnetic anomalies antipodal to lunar impact basins: Two-dimensional model calculations, *J. Geophys Res.*, *96* (B6), 9837-9846, 1991.

Hood, L.L., and G. Schubert, Lunar magnetic anomalies and surface optical properties, *Science*, *208*, 49-51, 1980.

Hood, L.L., and A. Vickery, Magnetic field amplification and generation in hypervelocity meteoroid impacts with application to lunar paleomagnetism, *Proc. Lunar Planet. Sci. Conf. 15th*, Part 1, *J Geophys. Res.*, *89*, suppl., C211-C223, 1984.

Hood, L.L., and C.R. Williams, The lunar swirls: Distribution and possible origins, *Proc. Lunar Planet. Sci. Conf.*, *19th*, 99-113, 1989.

Hood, L.L., P.J. Coleman, and D.E. Wilhelms, Lunar nearside magnetic anomalies, *Proc. Lunar Planet. Sci. Conf.*, *10th*, 2235-2257, 1979.

Hood, L.L., C.T. Russell, and P.J. Coleman, Contour maps of lunar remanent magnetic fields, *J.Geophys. Res.*, *86* (B2), 1055-1069, 1981.

Hood, L.L., A. Yingst, D.L. Mitchell, R.P. Lin, M. Acuna, and A. Binder, Higher-resolution mapping of lunar crustal magnetic fields: Correlation with albedo markings of the Reiner Gamma class, in *Workshop on "New Views on the Moon II: Understanding the Moon Through the Integration of Diverse Datasets"*, LPI contrib. *980*, pp. 28-29, Lunar and Planet. Inst., Livermore, Calif., 1999.

Johnson, J.R., S.M. Larson, and R.B Singer, Remote sensing of potential resources, 1, Near-side compositional properties, *J. Geophys. Res.*, *96* (E3), 18,861-18,882, 1991a.

Johnson, J R., S.M. Larson, and R.B. Singer, A reevaluation of spectral ratios for lunar mare TiO2 mapping, *Geophys. Res. Lett.*, *18* (11), 2153-2156, 1991b.

Johnson, P E., P.C. Pinet, and S D. Chevrel, Multispectral mixture modeling of the Apollo 15 landing site, in *Actes du Colloque national de Planétologie*, vol. 2, pp. S8-51, Univ. de Toulouse, Toulouse, France, 1994.

Johnson, T .V., J.A. Mosher, and D.L Matson, Lunar spectral units. A northern hemisphere mosaic, *Proc. Lunar Sci. Conf 8th*, 1013-1028, 1977.

Jolliff, B.L., Clementine UVVIS multispectral data and the Apollo 17 landing site: What can we tell and how well?, *J. Geophys. Res.*, *104* (E6), 14,123-14,148, 1999.

Lin, R.P., K.A. Anderson, and L.L. Hood, Lunar surface magnetic field concentrations antipodal to young large impact basins, *Icarus*, *74*, 529-541, 1988.

Lin, R.P., D.L. Mitchell, D.W. Curtis, K.A. Anderson, C.W. Carlson, J.

McFadden, M.H. Acuna, L.L. Hood, and A. Binder, Lunar surface magnetic fields and their interaction with the solar wind: Results from Lunar Prospector, *Science*, *281*, 1480-1484, 1998.

Lucey, P.G., G.J. Taylor, and E. Malaret, Abundance and distribution of iron on the Moon, *Science*, *268*, 1150-1153, 1995.

Lucey, P.G., D.T Blewett, and B.R. Hawke, Mapping the FeO and TiO2 content of the lunar surface with multispectral imagery, *J. Geophys. Res.*, *103* (E2), 3679-3699, 1998.

Martin, P.D., P.C. Pinet, S.D. Chevrel, and Y.H. Daydou, New methodology for spectral analyses at high spatial resolution: An example through the investigation of the Mare Humorum region of the Moon, (abstract), *Lunar Planet. Sci.*, *28th*, 877-878, 1997.

McEwen, A.S., A precise lunar photometric function (abstract), *Lunar Planet. Sci. 27th*, 841-842, 1996.

McEwen, A.S., L.R. Gaddis, G. Neukum, H. Hoffman, C.M. Pieters, and J.W. Head, Galileo observations of Post-Imbrium lunar craters during the first Earth-Moon flyby, *J. Geophys. Res.*, *98* (E9), 17,207-17,231,1993.

McKay, D., et al., Lunar regolith, in *Lunar Sourcebook*, edited by G. Heiken, D. Vaniman, and B.M. French, chap. 7, pp. 285-356, Cambridge Univ. Press, New York, 1991.

Meech, K.J., Physical properties of cometary nuclei (preprint IFA-97-38), paper presented at Asteroids, Comets, Meteors, 96 COSPAR Conference, Comm. On Space Prog. and Res., 10, Versailles, 1996.

Melosh, H.J., *Impact Cratering: A Geologic Process*, 245 pp., Oxford Univ. Press, New York, 1989.

Merényi, E., R.B. Singer, and J.S. Miller, Mapping of spectral variations on the surface of Mars from high spectral resolution telescopic images, *Icarus*, *124*, 280-295, 1996.

Morris, R.V., FMR and magnetic studies of Luna 24 soils and >1 mm soil particles, in *Mare Crisium. The view From Luna 24*, edited by R.B. Merrill and J.J. Papike, pp. 117-123, Pergamon, New York, 1978.

Mustard, J., and J.E. Hays, Effects of hyperfine particles on reflectance spectra from 0.3 to 25 micron, *Icarus*, *125*, 145-163, 1997.

Mustard, J., and J.W. Head, Buried stratigraphic relationships along the southwestern shores of Oceanus Procellarum, *J. Gephys. Res.*, *101* (E8), 18,913-18,925, 1996.

Nozette, S., et al., The Clementine mission to the Moon: Scientific overview, *Science*, *266*, 1835-1839, 1994.

O'Keefe, J D , and T.J. Ahrens, Cometary and meteorite swarm impact on planetary surfaces, *J. Geophys. Res.*, *87* (B8), 6668-6680, 1982.

Papike, J.J., S.B. Simon, and J.C. Laul, The lunar regolith: Chemistry, mineralogy and petrology, *Rev. Geophys.*, *20*, 761-826, 1982.

Pieters, C.M , Composition of the lunar highland crust from near-infrared spectroscopy, *Rev. Geophys.*, *24*, 557-578, 1986.

Pieters, C.M., Compositional diversity and stratigraphy of the lunar crust derived from reflectance spectroscopy, in *Remote Geochemical Analysis: Elemental and Mineralogical Composition*, edited by C.M. Pieters and P.A.J Englert, pp. 309-339, Cambridge Univ. Press, New York, 1993.

Pieters, C.M., and T.B. McCord, Characterization of lunar mare basalt types, I., A remote sensing study using reflection spectroscopy of surface soils, *Proc. Lunar Sci. Conf.*, *7th*, 2677-2690, 1976

Pieters, C.M., E.M. Fisher, O. Rode, and A. Basu, Optical effects of space weathering: The role of the finest fraction, *J. Geophys. Res.*, *98* (E11), 20,817-20,824, 1993.

Pinet, P.C., S.D. Chevrel, and V.V. Shevchenko, High resolution UV-VIS-near infrared spectro-imaging data of Reiner Gamma Formation, (abstract), *Lunar Planet. Sci.*, *23th*, 1077-1078, 1992

Pinet, P.C . S.D. Chevrel, and P. D. Martin, Copernicus. A regional probe of the lunar interior, *Science*, *260*, 797-801, 1993

Pinet, P C., V V Shevchenko, S.D. Chevrel, F. Bellagh, and C. Rosemberg, Reiner Gamma Formation: Optical, spectroscopic and polarimetric properties from Clementine and Earthbased data, (abstract), *Lunar Planet. Sci.*, *26th*, 1125-1126, 1995a.

Pinet, P.C., P.D. Martin, F. Costard, S.D. Chevrel, Y.H. Daydou, and P.E. Johnson, Aristarchus plateau Clementine spectro-imaging and geological inferences, (abstract), *Lunar Planet. Sci.*, *26th*, 1123-1124, 1995b.

Pinet, P.C., F. Costard, S.D. Chevrel, P.D. Martin, F. Bellagh, and J. Blamont, Aristarchus plateau spectral mapping from Clementine and telescopic high-resolution spectro-imaging data (abstract), *Lunar Planet. Sci.*, *27th*, 1037-1038, 1996.

Pinet, P.C., V.V. Shevchenko, and S.D. Chevrel, Reiner Gamma Formation from Clementine UV-VIS spectro-imaging data: The lunar chronology and iron content (abstract), *Lunar Planet. Sci.*, *28th*, 1115-1116, 1997.

Pinet, P.C., V.V. Shevchenko, S.D. Chevrel, and Y.H. Daydou, Local and regional lunar regolith characteristics at Reiner Gamma Formation (abstract), *Lunar Planet. Sci., 29th,* 1372-1373, 1998.

Rettig, T.W., M.J. Mumma, G.J. Sobczak, J.M. Hahn, and M. Di Santi, The nature of comet Shoemaker-Levy 9 subnuclei from analysis of preimpact Hubble Space Telescope images, *J. Geophys. Res., 101* (E4), 9271-9281, 1996.

Schenk, P.M., et al., Cometary nuclei and tidal disruption: The geologic record of crater chains on Callisto and Ganymede, *Icarus, 121,* 249-274, 1996.

Schultz, P.H, and I.J. Snrka, Cometary collisions on the Moon and Mercury, *Nature, 284,* 22-26, 1980.

Shevchenko, V.V., Optical properties of Reiner Gamma magnetic anomaly on the Moon (abstract), *Lunar Planet. Sci., 15th,* 772-773, 1984.

Shevchenko, V.V., Ages and frequency of the most recent cometary falls on the Moon from the analysis of swirl patterns, *Astron. Rep Transl. Astron. Zh., 71* (6), 935-943, 1994.

Shevchenko, V.V., The impact record of disrupted comets on the moon, (abstract) *Lunar Planet. Sci., 28th,* 1305-1306, 1997.

Shevchenko, V.V., P.C. Pinet, and S.D. Chevrel, Remote-sensing studies of immature lunar soils (Reiner-Gamma Formation), *Sol. Sys. Res.* (Eng. Transl.), *27* (4), 310- 321, 1993.

Smith, M.O., S.L. Ustin, J.B. Adams, and A.R. Gillespie, Vegetation in deserts, I, A regional measure of abundance from multispectral images, *Remote Sens. Environ., 31,* 1-26, 1990a.

Smith, M.O., S.L. Ustin, J.B. Adams, and A.R. Gillespie, Vegetation in deserts, II, Environmental influences on regional abundance, *Remote Sens. Environ., 31,* 27-52, 1990b.

Srnka, L.J., and P.H. Schultz, A cometary origin of Reiner-Gamma magnetic anomalies (abstract), *Lunar Planet. Sci., 11th,* 1076-1078, 1980

Starukhina, L.V., and I.G. Shkuratov, Particle size dependence of spectral slope and the depth of absorption bands: Implication for lunar soils, paper presented at Vernadsky-Brown Microsymposium *24,* sponsored by the Russian National Committee of Geologists and International Union of Geological Sciences (I.U.G.S.), Moscow, 1996.

Sunshine, J.M., C.M. Pieters, and J.W. Head, New evidence for compositional diversity at Marius Hills from Galileo multi-spectral imaging, chapter 1, Ph.D. thesis, Brown Univ., Providence, R.I., 1994.

Tompkins, S, Central peaks of impact craters as probes of lunar crustal composition: Results from laboratory and remote spectral data, Ph.D. dissertation, 246 pp., Brown Univ., Providence, R.I., 1997.

Tompkins, S., J.F. Mustard, C.M. Pieters, and D.W. Forsyth, Semi-objective determination of lithologic endmembers in a geologic environment (spectral mixture analysis) (abstract), *Lunar Planet. Sci., 25th,* 1407-1408, 1994.

Weitz, C.M., and J.W. Head III, Spectral properties of the Marius Hills volcanic complex and implications for the formation of lunar domes and cones, *J. Geophys. Res., 104* (E8), 18,933-18,956, 1999.

S.D. Chevrel, Y. Daydou, P.C. Pinet and C. Rosemberg, Laboratoire de Dynamique Terrestre et Planétaire (UMR 5562/CNRS/Université Paul Sabatier), Groupe de Recherche de Géodésie Spatiale, Observatoire Midi-Pyrénées. Toulouse, France. (Patrick.Pinet@cnes.fr; Serge. Chevrel@cnes.fr; Yves.Daydou@cnes.fr; Christine.Rosemberg@cns.fr)

V.V. Shevchenko, Sternberg Astronomical Institute. Moscow 119899. Russia. (shev@sai.msu.ru)